ACS OMEGA

Open Access

http://pubs.acs.org/journal/acsodf

Article

Erosion Investigation of Dimple Wall using Erosion-Coupled Dynamic Mesh

Libo Ren, Xiangyi Long, Xiaowei Wang, Hailan He, Manli Zhang, and Hao Lu*

Cite This: *ACS Omega* 2023, 8, 39303−39314

Read Online

ACCESS | Metrics & More | Article Recommendations

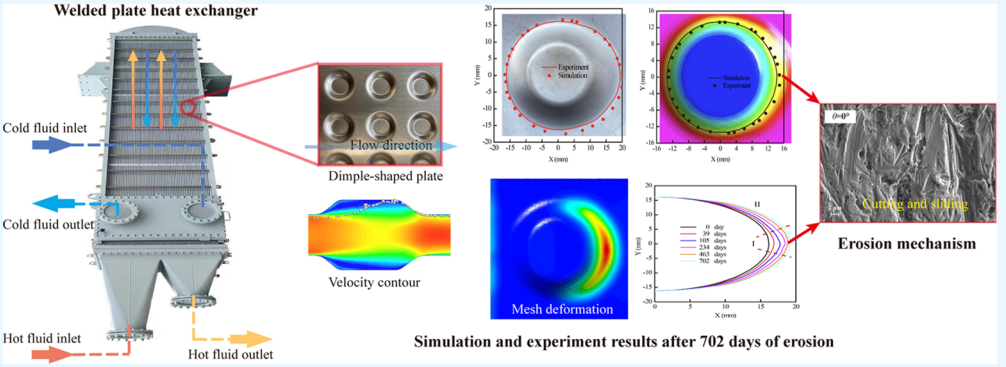

ABSTRACT: The erosion of the dimple walls is investigated experimentally and numerically. A mathematical simulation framework was proposed to describe quantitatively the morphological evolution of the dimple wall quantitatively. As the wall shape continues to evolve, the wall shear stress, mesh deformation, and erosion rate would decrease and gradually tend to be constant. Two distinct regions have been identified along the dimple's windward wall surface: the wall's central area and the lateral area. In the central region, the wall profile flare occurs mainly in the early stage. In the lateral region, profile flare occurs mainly in the later stages of erosion. The microhardness of the wall surface shows a positive correlation with the erosion rate. The liquid−solid two-phase impinges on the wall at a smaller angle, and the wall material removal process is mainly based on the microcutting and slip mechanism. The results provide theoretical implications for the design of dimple-shaped, wide-channel welded plate heat exchangers.

1. INTRODUCTION

Wide channel welded plate heat exchangers have been widely used in chemical, metallurgical, and electric power industries because of their high heat transfer efficiency, small footprint, and compact structure. Because of the contactless flow channel spacing, wide-channel welded plate heat exchangers have been commonly used for heat transfer of highly viscous media containing fibers and solid particles. As one of the highly efficient heat transfer plate types with enhanced heat transfer characteristics, dimple-shaped plates are a common plate type for wide-channel welded plate heat exchangers. The current research on dimple-shaped plates is mainly focusing on examining the influence laws of geometric parameters on heat transfer performance, such as smooth and staggered rows,[1,2] dimple depth,[2] dimple diameter,[1,3] dimple shape,[4,5] flow channel height,[6] etc. Yu et al.[7] showed that the downstream eccentric dimple structure has almost no stagnation zone in the heat transfer channel and has better enhanced heat transfer performance than the symmetric dimple structure channel. Under turbulent flow conditions, numerical simulation results obtained by Isaev et al.[8] showed that the heat transfer performance of ellipsoidal dimple structure flow had been improved by 10% over the spherical dimple structure. When a wide channel welded plate heat exchanger is used for thin particle liquid−solid two-phase heat transfer conditions and operates at high flow rates, solid particles would inevitably cause erosion of the dimple wall surface and lead to equipment failure. Under such circumstances, the study of dimple wall erosion is practically more significant.

The study of the movement patterns of solid particles in the liquid−solid two-phase flow field, the mutual impact process between the particles and the heat exchange surface, and the erosion patterns is of great significance to guide the design and operation of the equipment and, consequently, to reduce wear effectively. The studies on the erosion characteristics of

Received: July 5, 2023
Accepted: September 27, 2023
Published: October 13, 2023

liquid−solid two-phase have proliferated, primarily focusing on the particle size,[9,10] particle morphology,[11,12] particle and target hardness,[13] particle impact angle[14,15] and velocity,[15,16] temperature,[17,18] development of erosion models and numerical simulation frameworks,[19−21] etc. In recent years, with the rapid development of computer technology and testing techniques, the study of liquid−solid two-phase erosion characteristics has gradually moved from macroscopic to microscopic. For instance, Yu et al.[22] constructed a fluid-particle erosion model within the framework of Euler−Euler multiphase flow and extensively investigated the effect of the elastic recovery coefficient on erosion. Based on the combination of experimental studies and numerical simulations, H. Arabnejad et al.[23] obtained the effect of particle hardness on erosion patterns. Although numerous studies exist on the erosion characteristics of liquid−solid phases, extant research has mainly focused on circular pipe elbows with inner diameters larger than 50.6 mm or open-space jet conditions, and studies on the erosion characteristics of dimple walls are scant.

The mainstream numerical simulation methods of erosion have predominantly adopted the wall static-state method, in which the wall shape is retained fixed as the wall is exposed to the liquid−solid flow. However, it is worth noting that the change in the wall morphology caused by erosion is a dynamic process. Therefore, the static-state method does not agree with the actual situation. With the rapid development of numerical simulation technology in the past four-five years, the numerical simulation technique of erosion-coupled dynamic mesh has emerged. With such technology, the geometry of the wall structure changes alongside particle impacts. For example, Adedeji et al.[24] established a numerical simulation framework of erosion-coupled dynamic mesh to study the effect of wall roughness on erosion characteristics. Nguyen et al.[25] used the erosion-coupled dynamic mesh technique to numerically simulate the morphological changes of specimens under jet conditions, and their study showed that the erosion rate gradually decreased with the progress of erosion. The erosion-coupled dynamic mesh numerical simulation technique provides a new perspective for the study of erosion. However, to date, the application of this technique to the study of the erosion characteristics of dimple walls has rarely been reported.

In this study, we adopted a combination of experiments and numerical simulations to study the erosion characteristics of the dimple walls. Within the framework of ANSYS Fluent 2021 R1 software, we constructed a mathematical framework, integrating four CFD (Computational Fluid Dynamics)-DPM (Discrete Phase Model)-erosion-coupled dynamic mesh models. We validated and calibrated the accuracy of the constructed mathematical model on the experimental data. Then, the above model was used to study the hydrodynamic properties of the liquid−solid two-phase fluid in the channel composed of dimple walls, the deformation properties of the wall mesh, and the erosion properties. Additionally, in order to provide a basis for the design and operation of dimple-shaped wide-channel welded plate heat exchangers, we further explored the microscopic erosion failure mechanism of the wall surface. It is worth noting that the physical field information, such as instantaneous erosion rate, instantaneous impact velocity, instantaneous impact angle, and instantaneous impact mass flow, was obtained by the User-defined function (UDF) secondary development code.

2. EXPERIMENTAL CAMPAIGN

2.1. Experimental Setup. The liquid−solid two-phase erosion experimental setup is shown in Figure 1, which mainly

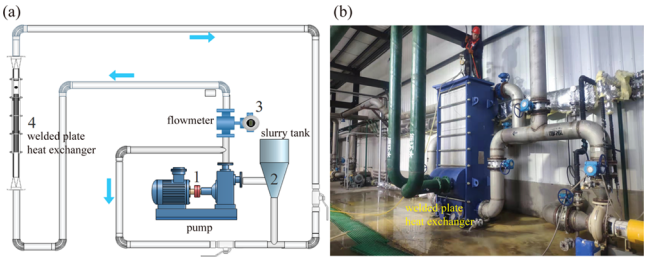

Figure 1. Experiment setup: (a) sketch of the erosion test facility; (b) photo of wide channel plate heat exchanger.

contains a pump, slurry tank, electromagnetic flow meter, welded plate heat exchanger, valve, and several stainless pipelines. The electromagnetic flow meter is used to measure the volumetric flow rate with a range of 0 to 700 m^3/h and an accuracy of 0.5%. The particles in the slurry tank are in full suspension, and the solid phase volume fraction is about 0.5%. The welded plate heat exchanger consists of several vertical rectangular channels with dimple walls. The channel inlet is equipped with a liquid distribution device, whose main function is to disperse the flow evenly over the width.

During the experimental process, the slurry in the slurry tank is pressurized by the pump and enters the system in two ways. One way is the main way, which enters the welded plate heat exchanger after measuring the volume with an electromagnetic flow meter. The other way is the bypass. The slurry of the two paths is mixed at the bottom of the tank and enters the slurry tank, forming a liquid−solid two-phase circulation flow. The main and bypass valves can be adjusted together to precisely control the slurry flow in the welded plate heat exchanger.

2.2. Dimple Wall. The dimple-shaped plate inside the welded plate heat exchanger and the cross-sectional line schematic of the dimple structure are shown, as shown in Figure 2. The initial thickness of the plate is 2.0 ± 0.02 mm, the material is SUS304 stainless steel, and the chemical composition is as follows: C ∼ 0.04%, Si ∼ 0.41%, Mn ∼ 1.1%, P ∼ 0.028%, S < 0.001%, Cr ∼ 18.32%, Ni ∼ 8.02%, N ∼ 0.04%. Fe is the balance component. The mechanical properties parameters are as follows: yield strength of 292 MPa, tensile strength of 695 MPa, elongation of 56%, and Vickers hardness of 1.62 GPa.

2.3. Sand Material. The sand in the liquid−solid two-phase medium is natural sand with SiO_2 as the main component and a density of 2450 kg/m^3. The particle size distribution and microscopic morphology are listed in Figure 3. The particles are nonspherical, with a particle sphericity coefficient of 0.75 obtained by image processing techniques.

3. MATHEMATICAL MODEL

3.1. Liquid Phase Governing Equation. Within the Eulerian framework, the three-dimensional liquid-phase flow field is described by using a liquid-phase governing equation based on local averaging and taking the liquid−solid interactions into consideration.

$$\frac{\partial(\rho)}{\partial t} + \nabla\cdot(\rho \boldsymbol{u}) = 0 \quad (1)$$

https://doi.org/10.1021/acsomega.3c04805
ACS Omega 2023, 8, 39303−39314

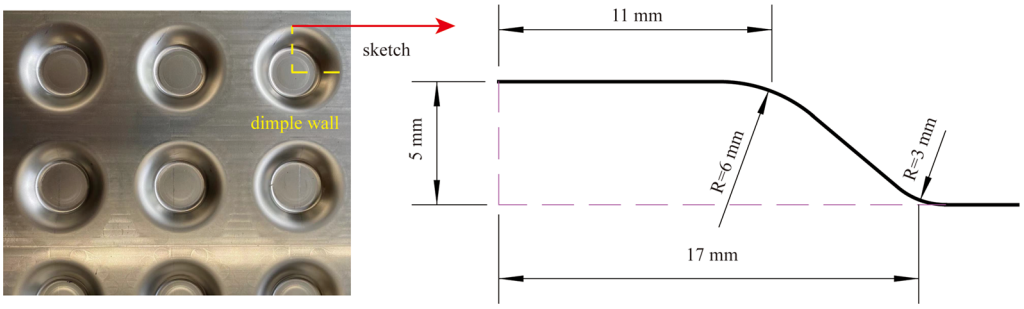

Figure 2. Sketch of the dimple wall

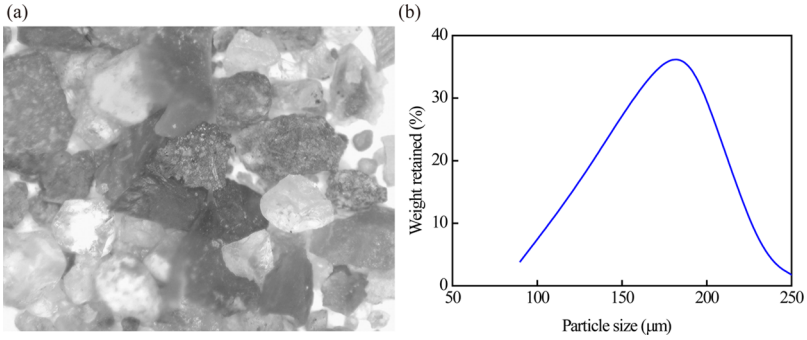

Figure 3. (a) Morphology of sand particles; (b) size distribution of sand particles.

$$\frac{\partial(\rho \boldsymbol{u})}{\partial t} + \nabla\cdot(\rho \boldsymbol{u}\boldsymbol{u}) = -\nabla P + \nabla\cdot(\tau) - S_{\mathrm{p}} + \rho \boldsymbol{g} \tag{2}$$

where ρ is the density, $\boldsymbol{u}$ is the velocity vector, $\boldsymbol{g}$ is the acceleration of gravity, P is the pressure, and $\boldsymbol{\tau}$ is the stress tensor. Based on Newton's third law, the liquid−solid interaction term $\boldsymbol{S}_{\mathrm{p}}$ in the mesh containing N particles is given by

$$S_{\mathrm{p}} = \frac{1}{V_{\mathrm{cell}}}\sum_{i=1}^{N} F_{\mathrm{d},i} \tag{3}$$

where $\boldsymbol{F}_{\mathrm{d},i}$ is the traction force of the liquid phase acting on particle i.

The liquid-phase turbulent energy and turbulent dissipation rate in the liquid−solid two-phase flow field are described using Standard k−ε.

$$\frac{\partial(\rho_{\mathrm{f}} k)}{\partial t} + \nabla\cdot(\rho_{\mathrm{f}} \boldsymbol{u}_{\mathrm{f}} k) = \nabla\cdot\left(\left(\mu_{\mathrm{f}} + \frac{\mu_{t,\mathrm{f}}}{\sigma_{\mathrm{k}}}\right)\nabla k\right) + G_{\mathrm{k}} - Y_{\mathrm{k}} + S_{\mathrm{k}} \tag{4}$$

$$\frac{\partial(\rho\varepsilon)}{\partial t} + \nabla\cdot(\rho \boldsymbol{u}\varepsilon) = \nabla\cdot\left(\left(\mu + \frac{\mu_{\mathrm{t}}}{\sigma_{\varepsilon}}\right)\nabla\varepsilon\right) + G_{\varepsilon} - Y_{\varepsilon} + D_{\varepsilon} + S_{\varepsilon} \tag{5}$$

where k is the turbulent energy, ε is the turbulent dissipation rate, μ_t is the turbulent viscosity, σ_{k} and σ_{ε} are the turbulent Prandtl numbers in the k and ε equations, which take the values of 1.0 and 1.3, respectively, G_{k} and G_{ε} are the generating terms, Y_{k} and Y_{ε} are the dissipation terms, D_{ε} is the cross-diffusion term, and S_{k} and S_{ε} are the source terms of the turbulent energy and turbulent dissipation rate, respectively.

3.2. Particle Phase Governing Equations.

In the Lagrangian framework, particles are treated as particle packets (Parcel), each of which represents several real particles. The velocity of the dispersive particle packet is solved by Newton's second law, and its position is updated by integrating the equations of motion. The equation of motion control for a rigid, nonspherical particle packet is given by

$$m_{\mathrm{p}}\frac{\mathrm{d}\boldsymbol{u}_{\mathrm{p}}}{\mathrm{d}t} = \frac{\pi d_{\mathrm{p}}^3 \rho_{\mathrm{p}}}{6}\left[\frac{\boldsymbol{g}(\rho_{\mathrm{p}} - \rho)}{\rho_{\mathrm{p}}} + F_{\mathrm{d,p}}\right] \tag{6}$$

where the subscript p denotes a solid particle, m is the mass of the particle, and $\boldsymbol{g}$ is the acceleration of gravity. $\boldsymbol{F}_{\mathrm{d,p}}$ is calculated as

$$F_{\mathrm{d,p}} = \frac{18\mu C_{\mathrm{D}}\mathrm{Re}_{\mathrm{p}}}{24\rho_{\mathrm{p}} d_{\mathrm{p}}^2}(\boldsymbol{u} - \boldsymbol{u}_{\mathrm{p}}) \tag{7}$$

where μ is liquid phase viscosity, d_{p} is particle diameter, and Re_{p} is particle Reynolds number, which is defined as

$$Re_{\mathrm{p}} \equiv \frac{\rho d_{\mathrm{p}}|\boldsymbol{u}_{\mathrm{p}} - \boldsymbol{u}|}{\mu} \tag{8}$$

and C_{D} is the drag coefficient for nonspherical particles, given as

$$C_{\mathrm{D}} = \frac{24}{Re_{\mathrm{p}}}(1 + b_1 Re_{\mathrm{p}}^{b2}) + \frac{b_3 Re_{\mathrm{p}}}{b_4 + Re_{\mathrm{p}}} \tag{9}$$

$$b_1 = \exp(2.3288 - 6.4581\varphi + 2.4486\varphi^2) \tag{10a}$$

$$b_2 = 0.0964 + 0.5565\varphi \tag{10b}$$

$$b_3 = \exp(4.905 - 13.8944\varphi + 18.4222\varphi^2 - 10.2599\varphi^3) \tag{10c}$$

https://doi.org/10.1021/acsomega.3c04805
ACS Omega 2023, 8, 39303−39314

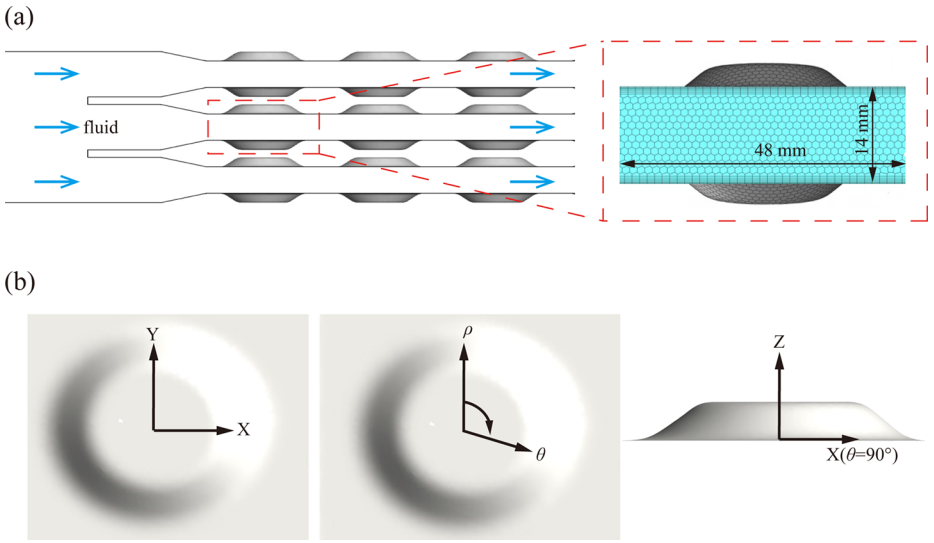

Figure 4. (a) Geometry and mesh generated for simulation; (b) Cartesian coordinate system and Axis coordinate system.

$$b_4 = \exp(1.4681 + 12.2584\varphi - 20.7322\varphi^2 + 15.8855\varphi^3) \quad (10d)$$

where φ is the particle sphericity coefficient, and the formula is calculated as

$$\varphi = \frac{s}{S} \quad (11)$$

where s is the surface area of spherical particles of the same volume as the nonspherical particles, and S is the surface area of nonspherical particles.

The particle turbulent dissipation characteristics are described by a random orbit model (Discrete Random Walk Model).[26] In order to balance the numerical simulation accuracy and computational effort, the number of particle random orbitals is set to 15.

3.3. Erosion Model. For individual solid particles, the Oka erosion model[16,27] was used to describe the erosion behavior of the sparse particle liquid−solid two-phase system on the wall in terms of the volumetric target wear rate (in mm^3/kg) caused by a unit mass of solid particles. The calculated expression is given by

$$E(\alpha) = g(\alpha)E_{90} \quad (12)$$

where $g(\alpha)$ represents the effect of impact angle and material hardness on the erosion rate calculated as

$$g(\alpha) = \sin\alpha^{n1}(1 + Hv(1 - \sin\alpha))^{n2} \quad (13)$$

$$\begin{aligned} n1 &= s1(Hv)^{q1}n2 \\ &= s2(Hv)^{q2}k2 \\ &= 2.3(Hv)^{0.038}n2 \\ &= s2(Hv)^{q2} \end{aligned} \quad (14)$$

where E_{90} is the erosion rate at an impact angle of 90° calculated as

$$E_{90} = K(Hv)^{k1}(V_p/V')^{k2}(D_p/D')^{k3} \quad (15)$$

For sand particles, the values of the constants in eqs 13 and 14 are as follows: $s1 = 0.71$, $s2 = 2.4$, $q1 = 0.14$, $q2 = -0.94$, $K = 65$, $k1 = -0.112$, $k3 = 0.19$, $V' = 104$ m/s, $D' = 326$ μm. From eq 12, we can see that with the increase of impact angle α, $g(\alpha)$ would increase first and then decrease; at the impact angle of 34.98°, $g(\alpha)$ reaches the maximum value. In addition, for SUS304 stainless steel, the Vickers hardness H_v is 1.62 GPa and the density ρ_t is 7980 kg/m^3.

The erosion rate (in $kg/(m^2{\cdot}s)$) is characterized by the mass wear rate of the target material per unit time and per unit area, and the equation is as follows:

$$E_h = \int_i^N \frac{M_p E(\alpha)}{\Delta A} = \frac{\int_1^N M_p g(\alpha)E_{90}}{\Delta A} = \frac{\sum_1^N M_p g(\alpha)E_{90}}{\Delta A} \quad (16)$$

where M_p is the mass of individual particles, ΔA is the wall mesh area.

The time averaging of E_h would give the time-averaged erosion rate in the time period from 0 to T, as shown in eq 17.

$$\bar{E}_h = \frac{\int_0^T E_h}{T} \quad (17)$$

3.4. Erosion-Coupled Dynamic Mesh Model. In the erosion process of liquid−solid dual-phase target materials, the geometric deformation of the target wall will change, which consequently causes the flow field and the erosion rate of solid particles on the target to change continuously. Eventually, the erosion process will change. In order to accurately simulate the impact of the wall boundary evolution process on the erosion rate, an erosion-dynamic mesh technique based on the quasi-steady-state method is introduced in this study. In this technique, the wall mesh node positions are updated based on the instantaneous erosion rate. Then, the flow field and the erosion rate field are recalculated based on the deformed mesh, realizing the coupling of CFD-DPM-erosion. In the erosion-dynamic mesh model, the deformation control equation of the wall mesh is given by

$$\Delta x = E_h \frac{\Delta T}{\rho_t} \quad (18)$$

where ΔT is the time step.

https://doi.org/10.1021/acsomega.3c04805
ACS Omega 2023, 8, 39303−39314

4. NUMERICAL SIMULATION METHOD

The experimental results show that the dimple walls near the inlet of the flow channel are the most susceptible to erosion failure. Additionally, the closer to the inlet area of the dimple wall surface, the faster the erosion will be. In order to fully consider the influence of the inlet effect on the erosion and to eliminate the sidewall effect, the model that has been used in the numerical simulation is shown in Figure 4a, in which the dimple wall in the red box is the object of study. To improve the convergence of the numerical simulation and computational robustness and to ensure that the height of the first mesh layer in the wall area is universally uniform, the discrete computational domain of Fluent Meshing software has been adopted. To facilitate the description of the different covariates, the postprocessing process establishes a Cartesian coordinate system and an axial coordinate system, respectively, as shown in Figure 4b. The liquid and solid phases flow along the X-axis/$\theta = 90°$ direction.

Based on the mesh-independence test, a 0.8 mm polyhedral mesh was used in the discrete computational domain. In Eulerian−Lagrangian numerical simulations, the first layer mesh height strongly affects the particle-wall interaction.[28] Therefore, a seven-layer prismatic mesh was laid near the wall to capture the flow boundary layer flow field information, and the first mesh height (~140 μm) in the wall region was slightly larger than the maximum particle radius.

The liquid and solid phases in the narrow channel are highly viscous solutions containing solid particles: liquid phase density 1050 kg/m^3, viscosity 21.0 cP, solid phase volume fraction 0.5% at the entrance, and solid particle density 2450 kg/m^3.

A mass flow inlet was used for the liquid phase inlet. The mass flow rate is 17.6 kg/s (converted from the experimental flow rate values). The flow direction is parallel to the inlet's normal direction. The escape boundary condition is used for the particles. The pressure exit boundary condition is used for the outlet. The particles are also subjected to the escape boundary condition. The 48 mm width direction is subjected to the periodic boundary condition. At the dimple wall boundary, no-slip boundary conditions are used for the liquid phase. The particle-wall interaction is considered, and the particle-wall interaction is an inelastic collision. The particle reflection velocity should be smaller than the incident velocity. The normal and tangential recovery coefficients for particle-wall collisions are shown below:[29]

$$e_n = 0.988 - 0.78\theta + 0.19\theta^2 - 0.024\theta^3 + 0.027\theta^4 \quad (19)$$

$$e_t = 1.0 - 0.78\theta + 0.84\theta^2 - 0.21\theta^3 + 0.28\theta^4 - 0.022\theta^5 \quad (20)$$

The liquid-phase flow field is calculated iteratively using the Coupled algorithm. The pressure, momentum, turbulent kinetic energy, and turbulent kinetic energy dissipation equations are chosen to be discretized in a second-order windward format with default relaxation factors. The particle phase is injected from the inlet surface into the computational domain, and the flow field is solved by using a two-way coupling of the liquid-phase flow field and the solid-phase motion field.

Based on the static mesh, the liquid-phase flow field is first simulated. After convergence, CFD-DPM two-way coupling is performed to solve the liquid-phase flow field and the particle field. Using the converged CFD-DPM coupled field as the initial field, the erosion-dynamic mesh coupled model is then initiated to numerically simulate the erosion field of the dynamic dimple wall. Specifically, the number of steps of dynamic mesh light compliance is set to 5. Using adaptive time steps, the minimum and maximum values of time steps are set to 1 and 86,400 s, respectively.

5. MODEL VALIDATION

5.1. Nguyen Q B Experiment. Nguyen et al. studied the erosion behavior of a liquid−solid two-phase medium consisting of water and sand particles on a SUS304 stainless-steel plate.[30] The liquid−solid two-phase medium was injected vertically into the stainless-steel plate through a 6.4 mm diameter nozzle. The vertical distance between the nozzle outlet and the steel plate is 12.7 mm, and the two-phase flow rate inside the nozzle is 30 m/s. The remaining parameters are presented in the literature.[30] A comparison of the erosion depth of the SUS304 stainless-steel plate at 5 and 30 min obtained from numerical simulations to the results of the literature[30] is shown in Figure 5. From the figure, we can

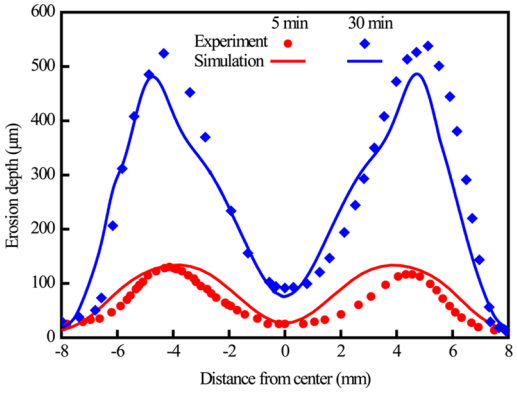

Figure 5. Profiles of the erosion depth.

observe that the radial erosion rate shows an "M" shape with respect to the radial direction. The maximum corrosion depth region is located in the radial range of 4.3 ~ 5.2 mm, and the erosion is milder when the center and radial distance are greater than 8 mm. The simulation results obtained from this article are consistent with the extant literature. The mathematical model constructed can decently describe the erosion behavior of the liquid−solid two-phase dilute particles and the evolution of the shape of the SUS304 stainless-steel walls.

5.2. Experiments in This Study. The surface morphology of the dimple-shaped plate obtained after 702 days of erosion and its 3D scan model are shown in Figure 6. The X/Y coordinate values of the wall shape curves of the dimple-shaped plate at $Z = 0.5$ and $Z = 2.5$ mm obtained from the experiments and numerical simulations are also shown in Figure 6. From Figure 6, we can observe that the windward wall surface shows obvious erosion characteristics. The degree of mesh deformation in the numerical simulation matches well with the distribution of the experimental erosion pattern. These results suggest that the established mathematical model can decently describe the erosion behavior of the thin particle liquid−solid two-phase medium on the dimpled wall surface of SUS304 stainless steel.

https://doi.org/10.1021/acsomega.3c04805
ACS Omega 2023, 8, 39303−39314

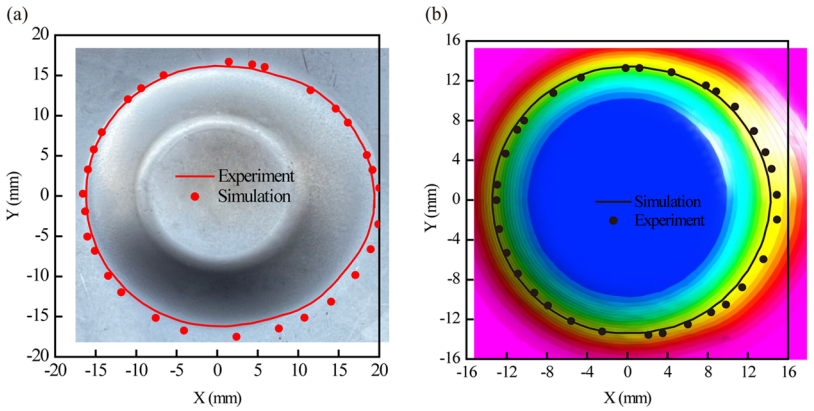

Figure 6. Failure plate and its 3-D scanning model: Curve profile of Z = 0.5 mm (a) and Z = 2.5 mm (b), flow direction is from left to right.

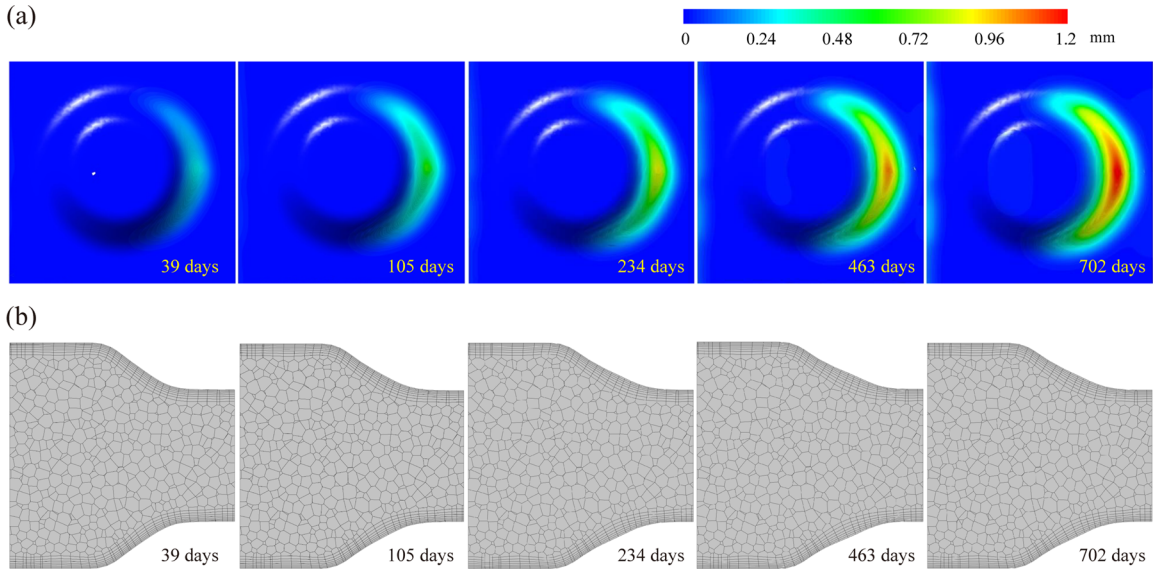

Figure 7. Evolution of the mesh on the dimple wall surface based on the erosion-coupled dynamic mesh technique: (a) contour of accumulated mesh deformation; (b) accumulated mesh deformation and the result of the dynamic meshing on the Y = 0 surface.

6. RESULTS AND DISCUSSION

6.1. Mesh Deformation Characteristics. The evolution contour of the cumulative displacement of the mesh on the dimple wall surface obtained based on the erosion-coupled dynamic mesh technique is shown in Figure 7a. As can be seen from Figure 7a, the cumulative displacement of the mesh on the windward side of the dimple wall surface increases with the erosion of the particles on the wall surface. Regardless of the amount of mesh displacement, the region of the maximum displacement value of the wall mesh is always located on the dimple windward wall surface, which intersects with the flat wall surface. In addition, the mesh displacement occurs first at the wall surface in the $\theta = 90°$ region in the axial coordinate system. Then the mesh movement of the wall surface in the nearby area is driven in both the circumference and axial directions. Finally, the overall displacement of the local windward wall mesh is achieved.

The evolution of the Y = 0 surface mesh obtained based on the erosion-coupled dynamic mesh technique in the Cartesian coordinate system is shown in Figure 7b. As can be seen from Figure 7b, there is a significant displacement of the windward mesh of the wall, while there is no significant change in the polyhedral mesh inside the calculation domain. The displacement of the wall surface mesh is achieved by moving the outermost prism mesh nodes outward and driving the expansion of other prism meshes in the nearby region.

In FLUENT software, the normal vector of the boundary mesh points outside the computational domain, and the face mesh moves outside the computational domain along its normal vector. The area of the boundary mesh is calculated by the normal vector. The area of the wall mesh is then used for erosion rate calculation. Therefore, the real-time update of the normal vectors of the wall boundary mesh becomes very important. After each DPM iteration calculation, the displacement of the outermost prism mesh is calculated and shifted according to that displacement. Then its normal vector is updated. The other parameter information stored in the wall mesh at the previous time step is interpolated into the wall mesh at the current time step, and the liquid phase flow field is recomputed for the entire computational domain. The cycle is repeated, and finally, an efficient coupling of the CFD-DPM-erosion-dynamic mesh model is achieved.

6.2. Flow Characteristics. The dimensionless Stokes number St describes the ratio of particle relaxation time to fluid characteristic time, which reflects the followership of the particles to the fluid and is calculated as

https://doi.org/10.1021/acsomega.3c04805
ACS Omega 2023, 8, 39303−39314

$$St = \frac{\rho_p d_p V_f}{18\mu_f} \quad (21)$$

The smaller the *St* number, the more the particle motion trajectory overlaps with the liquid phase flow line. The liquid phase velocity contour, streamline, and particle phase velocity contour are shown in Figure 8. From Figure 8, it can be seen

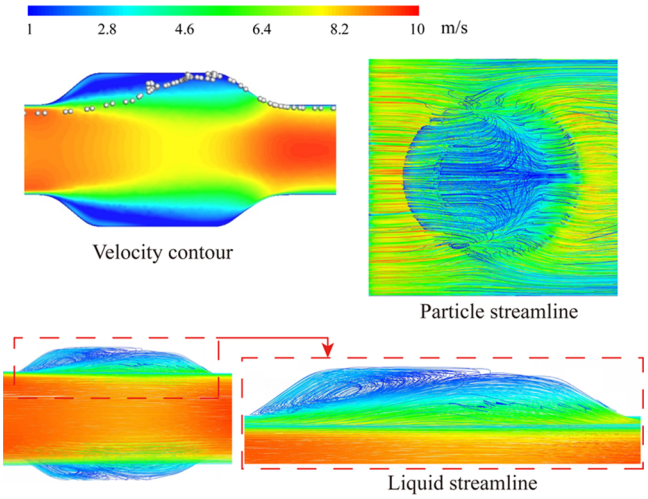

Figure 8. Flow field information on liquid phase and particle. Flow direction is from the left to right.

that the liquid phase velocity in the calculation domain is in the range 0−8.5 m/s. The particle local *St* number is in the range of 0−14.46. It indicates that the particles have good followership and the liquid phase flow field can significantly affect the wall erosion. It can also be seen from Figure 8 that the particles launched from the inlet surface under the action of high intensity turbulence of the liquid phase undergo pulsating motion and have the same magnitude of velocity moving forward as that of the liquid phase. The dimple structure then disrupts the original flow structure and changes the magnitude and direction of the liquid phase velocity. Some of the particles enter the interior of the dimple under the coercive action of the liquid phase, and the liquid phase and particles violently scour the windward side of the dimple wall and then merge into the main fluid. This eventually led to significant erosion in some areas of the windward side of the dimple wall.

The wall shear evolution contour obtained based on the erosion-coupled dynamic mesh is shown in Figure 9a. 0 day contour in Figure 9a shows the wall shear force contour at the undeformed moment of the mesh. The result is the same as the static mesh numerical simulation result. Comparing the 0 day contour with the other contour in Figure 9a, it can be seen that the wall shear contour obtained by the dynamic mesh technique is obviously different from the static mesh numerical simulation results. As the windward wall mesh moves to the outside of the computational domain, the interaction force between the liquid−solid phases and the wall surface weakens and the wall shear force continues to decrease. However, the instantaneous larger value of the wall shear force is always located on the dimple windward wall surface that intersects with the flat wall surface. At the end of the erosion, the influence of wall shape evolution on the degree of wall shear reduction is smaller, and the larger value of wall shear is maintained at about 1050 Pa. Since the parameters of wall shear, turbulent kinetic energy, and turbulent kinetic energy dissipation rate are all proportional to the liquid phase velocity.[31] As with wall shear stress, parameters such as turbulent kinetic energy and turbulent kinetic energy dissipation rate also respond accordingly to changes in the liquid phase velocity due to wall evolution.

6.3. Erosion Characteristics. The time-averaged erosion rate evolution contour obtained based on the erosion-coupled dynamic mesh is shown in Figure 9b. From Figure 9b, it can be seen that the deformation of the dimple wall surface has obvious directional and local severe characteristics. The degree of deformation matches well with the distribution of the erosion rate. The main manifestation is that the dimple windward wall surface as a whole expands unevenly outward, making the volume of the flow channel expand. The reason for this phenomenon is that the sudden narrowing of the flow channel increases the chance of collision between the particles and the wall surface so that the particles tend to collide head-on and deepen the degree of erosion of the dimple windward wall surface. Therefore, the root cause of the expansion of the channel volume is the gradual peeling of the wall material from the surface. Regardless of the deformation of the dimple wall surface, the instantaneous maximum deformation area is always located on the windward wall surface at the intersection with the flat wall surface. Erosion changes the structural morphology of the dimple windward wall surface and its collision characteristics with the particles (impact angle, impact velocity, impact frequency, etc.), slowing the subsequent deformation in this region. This eventually leads to a gradual decrease in the time-averaged erosion rate with the deformation of the wall structure. Zero days contour in Figure 9b shows the contour of the wall erosion rate at the undeformed moment of the mesh. This result is the same as the static mesh numerical simulation result. It can be seen that the erosion rate of the dimple wall surface obtained by the dynamic mesh technique is significantly lower than that of the static mesh numerical simulation by about 1 order of magnitude.

Factors such as the impact angle, impact velocity, and impact frequency of the particles (characterized using impact mass flow rate, i.e., the total mass of particles impacting on the wall microelements per unit time) are the most important parameters in determining the severity of erosion. Based on the transient mesh storage file, the distribution curves of the time-averaged erosion rate and each major parameter affecting the erosion rate along the circumference direction of the dimple wall were obtained by the UDF function within the secondary development framework of ANSYS Fluent 2021 R1, as shown in Figure 10. It can be seen that the mass flow rate (Eh, Figure 10a), flow rate (Figure 10b), velocity (Figure 10c), and angle (Figure 10d) of particles impacting the wall surface decrease to different degrees with the evolution of the wall shape. Under the combined effect of these factors, the wall erosion rate in this region is continuously reduced. As the wall morphology becomes smoother, the mass flow rate of particles hitting the dimple wall surface decreases significantly and varies little in the annular direction. Eventually, the distribution of the instantaneous erosion rate tends to be uniform in the circumference direction. In addition, in the region of θ = 75° to 90°, the mass flow rate of particles impinging on the wall surface increases with the increase of the θ angle. This is mainly due to the formation of a secondary flow in the region

https://doi.org/10.1021/acsomega.3c04805
ACS Omega 2023, 8, 39303−39314

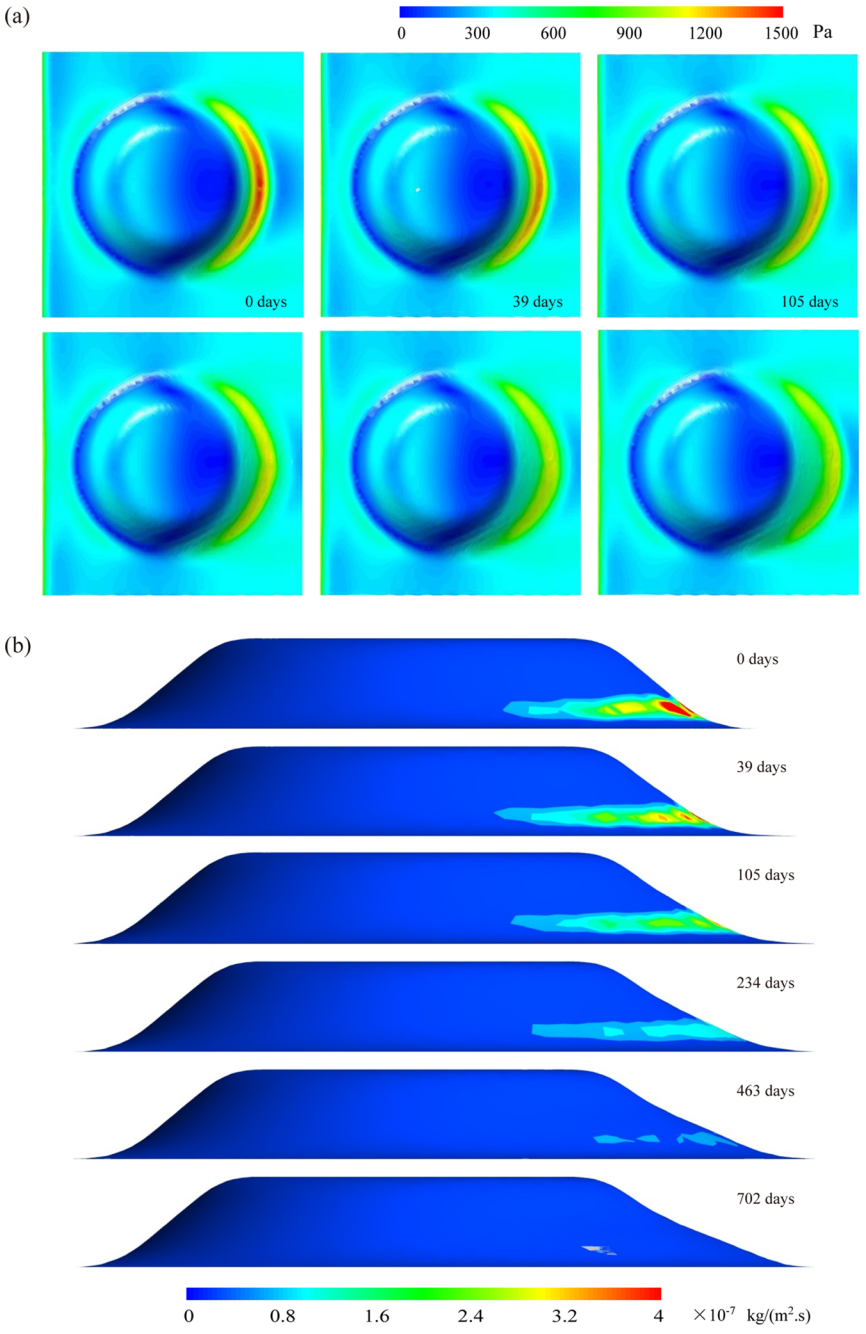

Figure 9. Evolution contour of wall shear stress (a) and time-averaged erosion rate (b).

near the windward wall of the nest as shown in Figure 11, which carries a large number of particles to the wall region near $\theta = 90°$.

The evolution curves of the dimple windward wall profile lines at $Z = 0.5$ and $Z = 2.5$ mm are shown in Figure 12. From Figure 12, it can be seen that the outward expansion of the profile line at $Z = 0.5$ and $Z = 2.5$ mm occurs mainly in the area of $X > 5$ mm, and the profile line shows a noncircular shape after deformation, not remaining circular. In the axial coordinate system, the windward wall surface is divided into two regions along the annulus. The central region is located in the range of $\theta = 90° \pm 15°$ and the lateral region is located in the range of $\theta = 0°\sim75°$ and $105°\sim180°$, which are recorded as the I region and II region, respectively. In I region, the extension of the wall surface occurs mainly at the beginning of the erosion. Then, the deformation becomes slower and slower. In II region, the extension of the wall surface mainly occurs in the late stage of erosion. As can be seen from Figure 9b and Figure 12, in the axial direction, profile flare mainly occurs in the windward wall area with $Z < 3.5$ mm, and in the annular direction, it mainly occurs in the area near $\theta = 90°$; the closer to these areas, the more drastic is the degree of wall profile flare. In addition, it can be inferred from Figure 12 that after the erosion proceeds to a certain extent, the wall profile line morphology no longer changes significantly as the particles strike the wall, which is consistent with the stable erosion state observed by Huttunen-Saarivirta, Head et al.[32,33]

The side of the dimple plate where erosion occurs is marked as the κ side, and the side where no erosion occurs is marked as the Π side. In the cylindrical coordinate system, the profile line

https://doi.org/10.1021/acsomega.3c04805
ACS Omega 2023, 8, 39303−39314

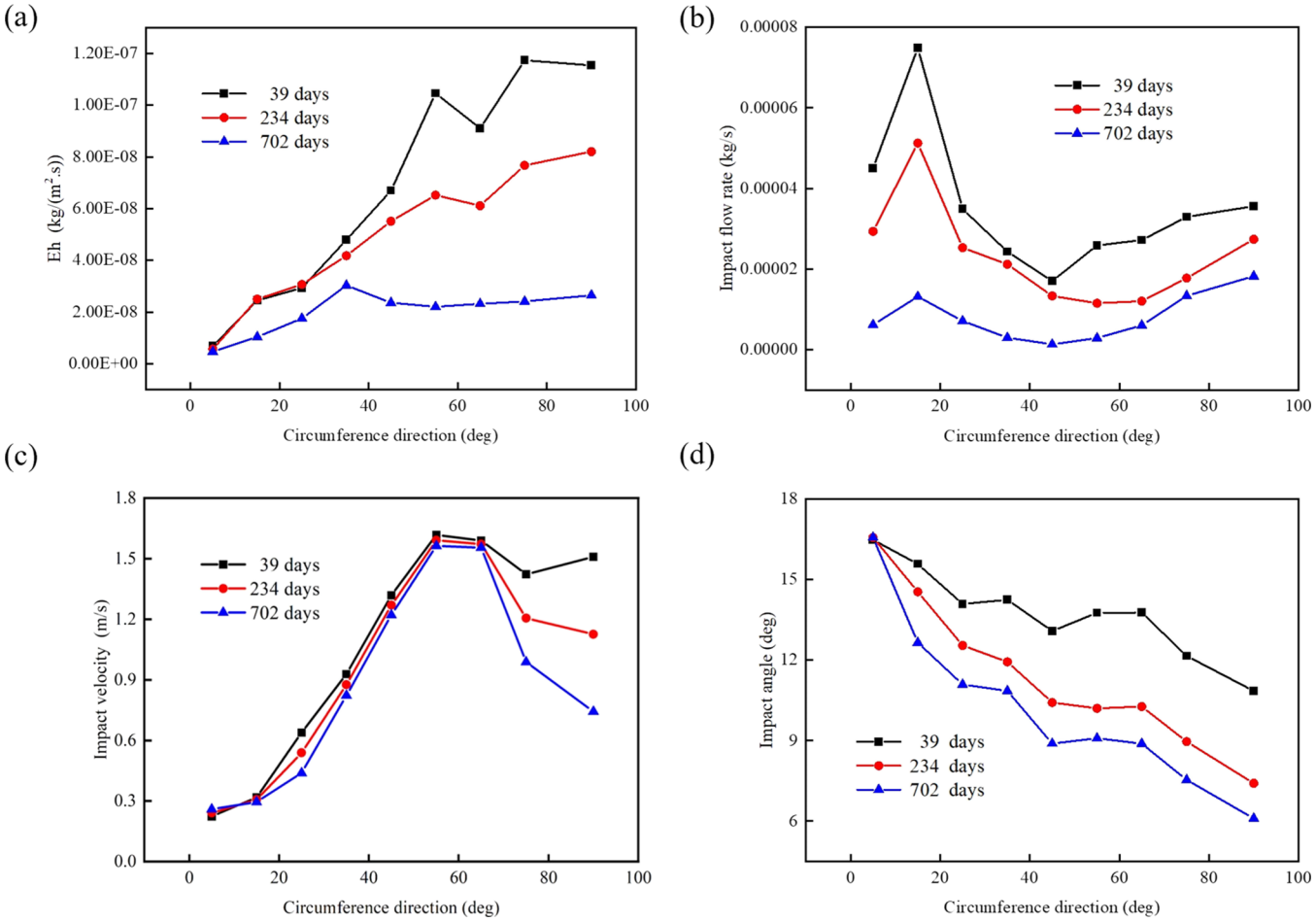

Figure 10. Profiles of the erosion rate and its influenced factors along the circumference direction: (a) erosion rate; (b) impact flow rate; (c) impact velocity; (d) impact angle.

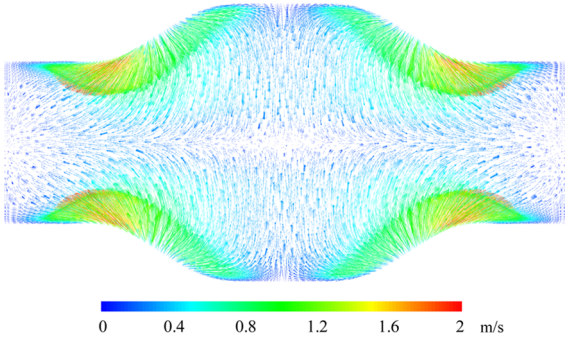

Figure 11. Velocity vector of secondary flow at X = 8.26 mm.

of the Π sidewall surface with θ being some certain value is extracted from the 3D scanning model shown in Figure 6. Then, the values of the ρ and Z coordinates of discrete points on this profile line are read at every 0.1 mm interval of ρ. Finally, the $Z = f(\rho)$ equation is obtained using the least-squares method of fitting a polynomial. The minimum distance between the coordinate point of each mesh center on the κ side wall and $Z = f(\rho)$ curve is solved, i.e., the wall thickness corresponding to each mesh node on the side of the κ wall. From the above, it is clear that the most severe erosion occurs on the wall surface in the region near $\theta = 90°$, which is the weakest region of the dimple-shaped plate. The evolution curve of the plate thickness on the $\theta = 90°$ line is given in Figure 13a. The evolution curve of the wall mesh displacement on the $\theta = 90°$ line is given in Figure 13b. From Figure 13a,b, it can be seen that the position of the minimum thickness of the dimple plate and the position of the maximum displacement of the wall mesh both move from the waist of the dimple wall surface to its intersection with the flat wall surface, and the rate of movement gradually decreased. From day 39 to day 702, the radial coordinate corresponding to the minimum thickness of the plate moved from 14.37 to 16.73 mm, and the radial coordinate corresponding to the maximum displacement of the wall mesh moved from 15.87 to 16.73 mm. Meanwhile, the minimum thickness of the plate was 0.97 mm at day 702, and the maximum displacement of the wall mesh was 1.23 mm, the sum of which was not equal to 2.0 mm. All these phenomena indicate that the curve evolution trends in Figure 13a,b are not completely consistent. The main reason for these phenomena is that wall mesh displacement does not always occur along the direction normal to the initial position of the wall on the κ side.

6.4. Microscopic Erosion Mechanism. Based on the analysis of macroscopic information such as shape and depth of wall erosion through experimental study and numerical simulation results, the microscopic morphology of the eroded wall surface and the erosion mechanism were further analyzed with the help of scanning SEM electron microscopy and micro hardness tester.

The SEM micrographs of the wall surface of the dimple-shaped plate after 702 days of erosion are presented in Figure

https://doi.org/10.1021/acsomega.3c04805
ACS Omega 2023, 8, 39303−39314

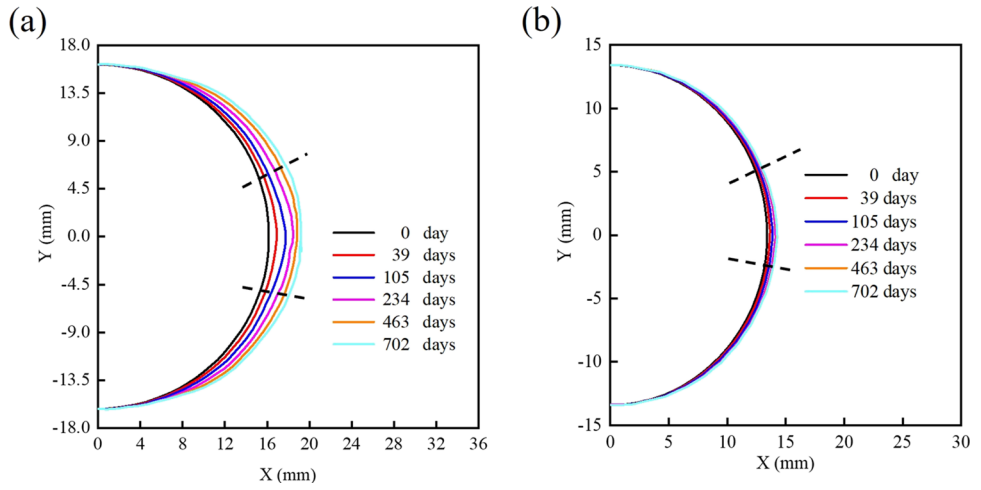

Figure 12. Morphological evolusion: (a) Z = 0.5 mm; (b) Z = 2.5 mm.

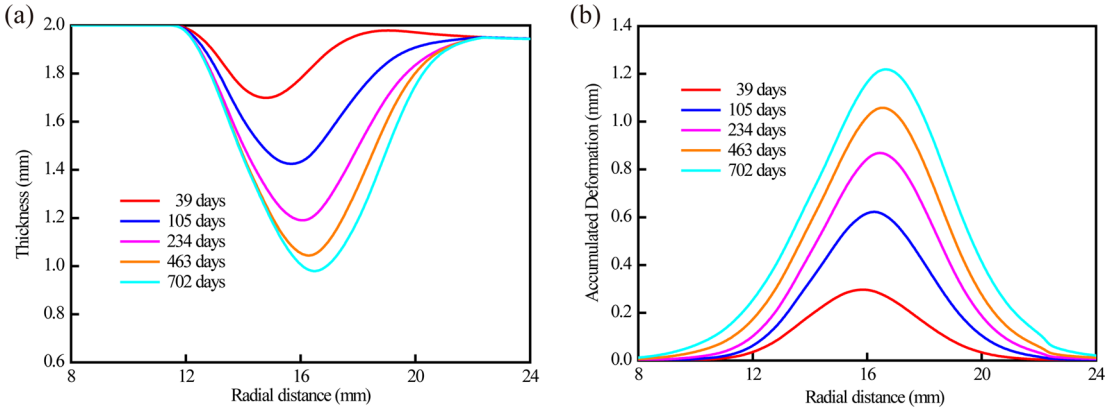

Figure 13. Evolution of sample thickness (a) and accumulated mesh deformation (b) on θ = 90°.

14a. Figure 14a shows that the surface of the dimple wall surface is uneven and shows directional micro plowing along the particle flow direction. This indicates that the damage to the dimple-shaped plate wall surface is mainly caused by the cutting and sliding mechanism of "microplasticity". In agreement with the results of the macroscopic analysis in Figure 10d, this erosion mechanism occurs mainly at smaller incidence angles of the particles.[34] When a solid particle impacts the surface of a dimple plate at a small impulse angle, the kinetic energy component along the plate normal to the plate causes the particle to press into the material surface and its large tangential kinetic energy component will make the solid particles cut the plate like a tool. Therefore, the strong ductile substrate produces transverse plastic flow at the contact point, cutting off a certain amount of microvolume material, as shown in the 2-μm resolution result in Figure 14a. The surface of the plate substrate is repeatedly impacted and squeezed by the solid particles, and the material surface is plastically deformed. By repeated rolling and formation of a band deformation layer, the edge of the layer cracks and flaps, forming obvious particle slip and cutting gullies. The lip is formed at the front edge of the gully. These lips are dislodged from the surface of the base material by the continuous impact of the particles. This results in the formation of larger material removal pits. The above process is repeated over and over again, causing the dimpled sheet profile to change continuously. Ultimately, a thickness reduction on the macroscopic scale of the sheet is achieved.

SEM micrographs of the dimple wall surface at Z = 2.0 mm on different annular angles are shown in Figure 14b. From Figure 14b, it can be found that the erosion gully direction shows an obvious regularity, i.e., mainly along the liquid−solid two-phase mainstream direction. However, there are also some erosion traces or gullies at a certain angle to the mainstream direction, especially in the θ = 0° to 30° region. From Figure 8, it can be seen that the particle trajectories in the region near θ = 90° are mainly along the liquid−solid mainstream direction at Z = 2 mm on the windward side of the dimple structure. In the area near θ = 0°, the particle trajectories are along the liquid−solid mainstream direction, while the rest of the particles are at an angle with the liquid−solid mainstream direction under the action of vortex coercion. Thus, it can be seen that the difference of particle movement trajectories in different regions is the main reason for the difference of the gully direction in the circumferential angle.

The surface microhardness distribution curve along the radial direction of the θ = 90° dimple wall surface at 702 days is shown in Figure 15. As can be seen from Figure 15, the maximum hardness is located near the area of the maximum erosion rate, and the hardness of the target surface shows a positive correlation with its erosion rate. The microhardness of the flat wall surface and the round wall surface in the center of the dimple structure is around 245 HV0.2. However, the

https://doi.org/10.1021/acsomega.3c04805
ACS Omega 2023, 8, 39303−39314

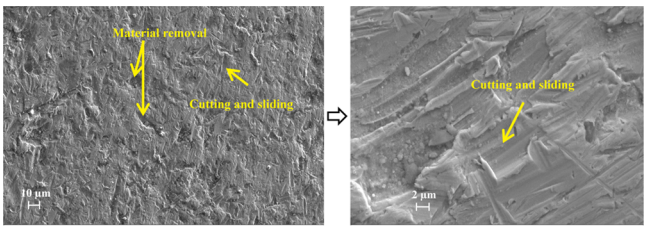

(a) Micro-cutting and micro-sliding at low impact angles.

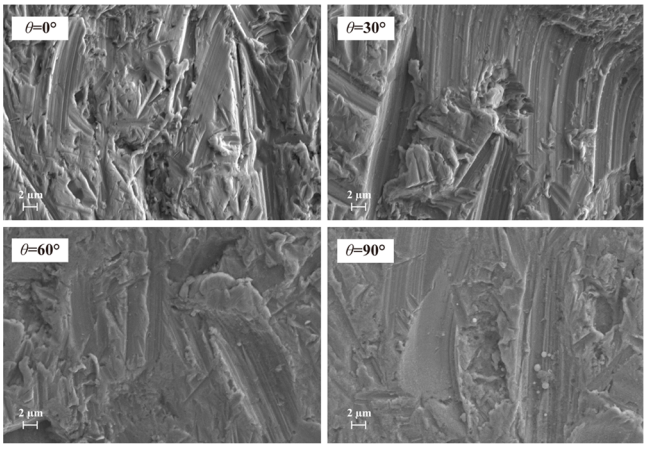

(b) Circumference angles on Z=2 mm. Flow direction is from bottom to top.

Figure 14. SEM micrographs of the erosion of the dimple wall surface after 702 days.

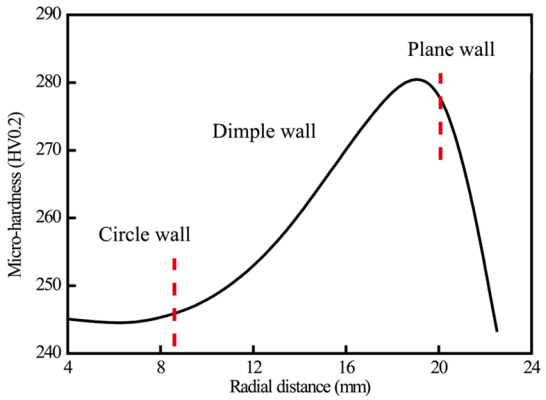

Figure 15. Microhardness along radial distance.

hardness of the windward wall surface of the dimple is much higher than the other parts, which is mainly due to the microscale cold work hardening effect on the surface layer caused by the repeated impact and cutting of the particles on the dimple windward wall.

7. CONCLUSIONS

While extensive research on liquid−solid two-phase erosion in round tubes and jet flow conditions has been conducted, the erosion investigation of dimple walls has been rarely reported. To close this research gap, in this study, we adopted CFD-DPM-erosion-coupled dynamic mesh numerical simulation in the framework of the secondary development of Fluent software to explore the characteristics of liquid−solid two-phase hydrodynamics, dimple wall mesh deformation and erosion, and the microscopic mechanism of wall erosion failure. Specifically, our results suggest that the numeric simulation model can describe the morphological evolution of the dimple wall surface in a quantitative and detailed way. Regardless of the evolution of the dimple wall shape, the maximum region of wall shear, mesh deformation, and erosion rate will always be on the dimple windward wall surface that intersects the flat wall surface. As the wall shape continues evolving, the wall shear, mesh deformation, and erosion rate would decrease and gradually tend to be constant. Two distinct regions have been identified along the dimple's windward wall surface: the wall's central area and the lateral area. In the middle region of the wall, wall profile flare occurs mainly in the early stages of erosion. In the lateral region, profile flare occurs mainly in the later stages of erosion. The microhardness of the wall surface shows a positive correlation with the erosion rate. The liquid−solid two-phase impinges on the wall at a smaller angle, and the wall material removal process is mainly based on the microcutting and slip mechanism.

AUTHOR INFORMATION

Corresponding Author

Hao Lu − *School of Mechanical and Power Engineering, East China University of Science and Technology, Shanghai 200237, P.R. China;* orcid.org/0000-0002-3516-8845; Email: luhao@ecust.edu.cn

Authors

Libo Ren − *Shanghai Heat Transfer Equipment Co., Ltd., Shanghai 201508, P.R. China*

Xiangyi Long − *School of Mechanical and Power Engineering, East China University of Science and Technology, Shanghai 200237, P.R. China*

Xiaowei Wang − *Shanghai Heat Transfer Equipment Co., Ltd., Shanghai 201508, P.R. China*

Hailan He − *Shanghai Heat Transfer Equipment Co., Ltd., Shanghai 201508, P.R. China*

Manli Zhang − *Shanghai Heat Transfer Equipment Co., Ltd., Shanghai 201508, P.R. China*

Complete contact information is available at: https://pubs.acs.org/10.1021/acsomega.3c04805

Notes

The authors declare no competing financial interest.

ACKNOWLEDGMENTS

This work is supported by the Shanghai Rising-Star Program (Grant No. 22QA1402600) and the National Natural Science Foundation of China (Grant No. 52000072).

REFERENCES

(1) Katkhaw, N.; Vorayos, N.; Kiatsiriroat, T.; Khunatorn, Y.; Bunturat, D.; Nuntaphan, A. Heat transfer behavior of flat plate having 45 ellipsoidal dimpled surfaces. *J. Case Stud. Therm. Eng.* **2014**, *2*, 67−74.

(2) Patel, I. H.; Borse, S. L. Experimental investigation of heat transfer enhancement over the dimpled surface. *Int. J. Eng. Sci. Technol.* **2012**, *4*, 3666−3672.

(3) Nascimento, I. P.; Garcia, E. C. Heat transfer performance enhancement in compact heat exchangers by using shallow square dimples in flat tubes. *J. Appl. Therm. Eng.* **2016**, *96*, 659−670.

(4) Elyyan, M. A.; Rozati, A.; Tafti, D. K. Investigation of dimpled fins for heat transfer enhancement in compact heat exchangers. *Int. J. Heat Mass Transfer* **2008**, *51*, 2950−2966.

(5) Abraham, J.; Maki, R. Hydrodynamics of laminar flow through dimpled pipes. *MOJ Civil Eng.* **2018**, *4*, 150−154.

https://doi.org/10.1021/acsomega.3c04805
ACS Omega 2023, 8, 39303−39314

(6) Shin, S.; Lee, K. S.; Park, S. D.; Kwak, J. S. Measurement of the heat transfer coefficient in the dimpled channel: Effects of dimple arrangement and channel height. *J. Mech. Sci. Technol.* **2009**, *23*, 624−630.
(7) Chen, Y.; Chew, Y. T.; Khoo, B. C. Enhancement of heat transfer in turbulent channel flow over dimpled surface. *Int. J. Heat Mass Transfer* **2012**, *55*, 8100−8121.
(8) Isaev, S.; Leontiev, A.; Mityakov, A.; Pyshnyi, I.; Usachov, A. Intensification of tornado turbulent heat exchange in asymmetric holes on a plane wall. *J. Eng. Phys. Thermophys.* **2003**, *76* (2), 266−270.
(9) Desale, G. R.; Gandhi, B. K.; Jain, S. C. Particle size effects on the slurry erosion of aluminium alloy (AA 6063). *J. Wear* **2009**, *266*, 1066−1071.
(10) Nguyen, V. B.; Nguyen, Q. B.; Zhang, Y. W.; Lim, C. Y. H.; Khoo, B. C. Effect of particle size on erosion characteristics. *J. Wear* **2016**, *348−349*, 126−137.
(11) Stachowiak, G. B. The effects of particle characteristics on three-body abrasive wear. *J. Wear* **2001**, *249*, 201−207.
(12) Walker, C. I.; Hambe, M. Influence of particle shape on slurry wear of white iron. *J. Wear* **2015**, *332-333*, 1021−1027.
(13) Desale, G. R.; Gandhi, B. K.; Jain, S. C. Slurry erosion of ductile materials under normal impact condition. *J. Wear* **2008**, *264* (3), 322−330.
(14) Abd-Elrhman, Y. M.; Abouet-Kasem, A.; Emara, K. M.; Ahmed, S. M. Effect of impact angle on slurry erosion behavior and mechanisms of carburized AISI 5117 steel. *J. Tribol.* **2014**, *136*, No. 011106.
(15) Islam, M. A.; Farhat, Z. N. Effect of impact angle and velocity on erosion of API X42 pipeline steel under high abrasive feed rate. *J. Wear* **2014**, *311*, 180−190.
(16) Oka, Y. I.; Okamura, K.; Yoshida, T. Practical estimation of erosion damage caused by solid particle impact part I: effects of impact parameters on a predictive equation. *J. Wear* **2005**, *259*, 95−101.
(17) Shimizu, K.; Xinba, Y.; Araya, S. Solid particle erosion and mechanical properties of stainless steels at elevated temperature. *J. Wear* **2011**, *271*, 1357−1364.
(18) Li, X.; Ding, H.; Huang, Z.; Fang, M.; Liu, B.; Liu, Y.; Wu, X.; Chen, S. Solid particle erosion-wear behavior of SiC−Si3N4 composite ceramic at elevated temperature. *J. Ceram. Int.* **2014**, *40*, 16201−16207.
(19) Ben-Ami, Y.; Uzi, A.; Levy, A. Modelling the particles impingement angle to produce maximum erosion. *J. Powder Technol.* **2016**, *301*, 1032−1043.
(20) Uzi, A.; Levy, A. On the relationship between erosion, energy dissipation and particle size. *J. Wear* **2019**, *428−429*, 404−416.
(21) Wang, Z. T. Erosion model for brittle materials under low-speed impacts. *J. Tribol.* **2020**, *142*, No. 074501.
(22) Yu, W.; Fede, P.; Climent, E.; Sanders, S. Multi-fluid approach for the numerical prediction of wall erosion in an elbow. *J. Powder Technol.* **2019**, *354*, 561−581.
(23) Arabnejad, H.; Shirazi, S. A.; Mclaury, B. S.; Subramani, H. J.; Rhyne, L. D. The effect of erodent particle hardness on the erosion of stainless steel. *J. Wear* **2015**, *332−333*, 1098−1103.
(24) Adedeji, O. E.; Duarte, C. A. R. Prediction of thickness loss in a standard 90° elbow using erosion-coupled dynamic mesh. *J. Wear* **2020**, *460−461*, No. 203400.
(25) Nguyen, V. B.; Nguyen, Q. B.; Liu, Z. G.; Wan, S.; Lim, C. Y. H.; Zhang, Y. W. A combined numerical−experimental study on the effect of surface evolution on the water-sand multiphase flow characteristics and the material erosion behavior. *J. Wear* **2014**, *319*, 96−109.
(26) ANSYS *ANSYS 2021 R1 Theory Guide*, 2021. DOI: 10.1021/acs.accounts.1c00016. Technical Report
(27) Oka, Y. I.; Ohnogi, H.; Hosokawa, T.; Matsumura, M. The impact angle dependence of erosion damage caused by solid impact. *J. Wear* **1997**, *203−204*, 573−579.
(28) Messa, G. V.; Wang, Y.; Negri, M.; Malavasi, S. An improved CFD/experimental combined methodology for the calibration of empirical erosion models. *J. Wear* **2021**, *476*, No. 203734.
(29) Zhang, Y.; Reuterfors, E. P.; Mclaury, B. S. Comparison of computed and measured particle velocities and erosion in water and air flows. *J. Wear* **2007**, *263*, 330−338.
(30) Nguyen, Q. B.; Lim, C. Y. H.; Nguyen, V. B.; Wan, Y. M.; Nai, B.; Zhang, Y. W.; Gupta, M. Slurry erosion characteristics and erosion mechanisms of stainless steel. *J. Tribol. Int.* **2014**, *79*, 1−7.
(31) Munson, B. R.; Rothmayer, A. P.; Okiishi, T. H. *Fundamentals of Fluid Mechanics*, 7th ed.; Wiley, 2012.
(32) Huttunen-Saarivirta, E.; Kinnunen, H.; Turiemo, J. Erosive wear of boiler steels by sand and ash. *J. Wear* **2014**, *317*, 213−24.
(33) Head, W.; Harr, M. The development of a model to predict the erosion of materials by natural contaminants. *J. Wear* **1970**, *15*, 1−46.
(34) Javaheri, V.; Porter, D.; Kuokkala, V. T. Slurry erosion of steel-Review of tests, mechanisms and materials. *J. Wear* **2018**, *15*, 248−273.

https://doi.org/10.1021/acsomega.3c04805
ACS Omega 2023, 8, 39303−39314